Probing core-electron orbitals by scanning transmission electron microscopy and measuring the delocalization of core-level excitations

Jong Seok Jeong,* Michael L. Odlyzko, Peng Xu, Bharat Jalan, and K. Andre Mkhoyan†

Department of Chemical Engineering and Materials Science, University of Minnesota, Minneapolis, Minnesota 55455, USA

(Received 17 August 2015; revised manuscript received 6 April 2016; published 26 April 2016)

By recording low-noise energy-dispersive x-ray spectroscopy maps from crystalline specimens using aberration-corrected scanning transmission electron microscopy, it is possible to probe core-level electron orbitals in real space. Both the $1s$ and $2p$ orbitals of Sr and Ti atoms in $SrTiO_3$ are probed, and their projected excitation potentials are determined. This paper also demonstrates experimental measurement of the electronic excitation impact parameter and the delocalization of an excitation due to Coulombic beam-orbital interaction.

DOI: 10.1103/PhysRevB.93.165140

I. INTRODUCTION

While all matter is comprised of atoms, our understanding of the electron orbitals that determine how those atoms behave is mostly based on theory or indirect evidence rather than on direct experimental measurements of electron density. Nevertheless, the mapping of electron densities in near-defect-free crystals has been demonstrated by structure factor determination using x-ray diffraction [1] and transmission electron microscopy (TEM) convergent beam electron diffraction [2–4]. Real-space characterization of the bonding electron orbitals of individual molecules and surface atoms has also been shown using atomic force microscopy [5,6] and scanning tunneling microscopy [7,8]. Going another level deeper and probing core-level electron orbitals, which are much smaller than bonding orbitals, presents a major experimental challenge. In this paper, we use scanning TEM (STEM) in conjunction with energy dispersive x-ray (EDX) spectroscopy to probe core-level electron orbitals in a $SrTiO_3$ (STO) crystal and furthermore to measure the impact parameter for excitation of a given orbital.

A STEM has proven an immensely powerful tool for imaging and chemically fingerprinting atoms. With the advent of aberration-correction [9,10], subangstrom STEM electron beams can be combined with EDX or electron energy-loss spectroscopy (EELS) to rapidly map solids with crisp atomic resolution [11–14]. Efforts to retrieve subatomic information from STEM-EELS spectrum images have been made [15,16], and the concept that core-level orbital information can be determined by deconvolving channeled STEM probes from spectrum images has also been discussed [16–19]. However, acquiring experimental low-noise, atomic-resolution maps for such analyses has been challenging, and the outcomes have been suitable only for basic qualitative interpretation. In this paper, using high-quality low-noise STEM-EDX maps of single-crystal STO, we demonstrate that STEM-EDX mapping can go beyond elemental profiling of whole atoms to quantitatively probe core-level electron orbitals. Details of experiments, analysis, and results are discussed below, including limitations of the method.

*Corresponding author: jsjeong@umn.edu

†Corresponding author: mkhoyan@umn.edu

II. EXPERIMENTAL PROCEDURES

For this paper, STO samples were used to verify the robustness of the proposed method. There are several advantages to using STO, not least the availability of high-quality single crystals, its multielement composition, and its high resistance to electron beam damage. While three different STO samples were examined, here, we focus on the results from one sample (the rest of the results can be found in the Supplemental Material [20]). The results from other samples will be presented at the end of the discussion for purposes of comparing results across independent data sets. Electron-transparent STEM specimens were prepared using combinations of mechanical wedge polishing [21], focused ion beam (FIB) lift out (FEI Quanta 200 3D), and Ar-ion milling (Fischione Model 1010 ion mill and Gatan precision ion polishing system). The thickness of the prepared TEM samples was estimated by the EELS log-ratio method [22,23], using a mean free path for bulk plasmon generation (for 300 keV electrons) in STO of $\lambda_p = 123$ nm [24]. Low-loss EELS data were acquired using a FEI Tecnai G2 F30 S/TEM equipped with a Gatan Enfina 1000 spectrometer. Measured thickness of the example specimen was 57.9 ± 11.0 nm (see Supplemental Material [20]).

An aberration-corrected (CEOS DCOR probe corrector) STEM (FEI Titan G2 60-300) equipped with a Schottky extreme field emission gun (X-FEG) and a monochromator was used. The microscope was operated at 300 keV. A standard high-contrast tuning specimen, a carbon diffraction grating replica coated with Au nanocrystals, was used for aberration measurement and correction (see Supplemental Material [20]). Fast Fourier transform (FFT) of the high-resolution high-angle annular dark-field (HAADF)-STEM images of the Au specimen indicates that the information limit after the correction was in the range of 0.7–0.8 Å. A study of corrector stability over the course of many hours showed that the resolution stably remains in the subangstrom range, showing that STEM-EDX experiments could be performed for at least 4 h without retuning the probe corrector (see Supplemental Material [20]). The collection angle of the HAADF detector was ranging from 50 mrad (inner) to 200 mrad (outer; the inner angle was calibrated and the outer angle was inferred from manufacturer specifications) and the convergent semiangle of the incident STEM probe α_{obj} was 24.5 mrad. Beam currents (I_p) in the range of 0.03–0.05 nA were used for HAADF-STEM imaging.

 ©2016 American Physical Society

The STEM images were acquired by 2048×2048 pixel^2 scans with dwell times of 2–6 μs pixel^{-1}.

The STEM-EDX maps were obtained using the FEI Super-X EDX detector system (four windowless silicon drift detectors (SDDs) integrated deeply into the objective lens) enabling higher x-ray count rates and more efficient x-ray collection than standard Si(Li) detectors [25]. Microscope conditions were kept the same as for HAADF-STEM imaging; an increased I_p in the range of 0.15–0.25 nA was used to obtain better signal. For each EDX map, we selected an area 32×32 Å^2 in size without any artifacts by specimen preparation, performing EDX acquisitions with drift correction frame by frame using Bruker Esprit 1.9 software. The dwell time was 4–8 μs pixel^{-1}. The overall acquisition time for every experiment varied according to how much the specimens drifted and was in the range of 115–317 s. The EDX maps with 128×128 pixel^2 and 256×256 pixel^2 scan sizes from each x-ray peak were interpolated to 600×600 pixel^2 size using a bilinear interpolation routine [26] for subsequent image processing. Mild beam damage effects (slight specimen thinning) were observed by HAADF imaging before and after STEM-EDX acquisitions (see Supplemental Material [20]). To extract net x-ray counts from each peak, elements of interest are selected, the Bremsstrahlung background is subtracted, each peak is fitted, and then the net x-ray counts from peaks in the windows are presented as corresponding elemental maps.

III. THEORETICAL PROCEDURES

A. Multislice simulations

Multislice simulations [27,28] were performed to model the interaction of the STEM focused electron beam with the STO crystal. Using the TEMSIM multislice package [29], incident aberration-corrected electron probes of various sizes were scanned over a ⟨100⟩-oriented STO supercell (15.62×15.62 Å^2 consisting of 4×4 unit cells). Both probe and transmission functions were calculated on a 1024×1024 pixel^2 grid, which resulted in a real space pixel size of $\Delta x = \Delta y = 0.0153$ Å and a reciprocal space pixel size of $\Delta k_x = \Delta k_y = 0.0640$ Å^{-1} (or $\Delta\alpha_x = \Delta\alpha_y = 1.26$ mrad for 300 keV electrons). Projected atomic potentials were calculated using the default parameterization tables of TEMSIM, and the slice thickness was made commensurate with the crystal structure ($\Delta z = 1.9525$ Å). Frozen phonon configurations were calculated as isotropic random displacements of the atomic positions according to the Einstein model [30], with root-mean-square (RMS) displacements 0.049, 0.035, and 0.045 Å for O, Ti, and Sr, respectively [31]. The HAADF-STEM image simulations were performed by forming two-dimensional (2D) images at various sample depths using a detector collection angles 50–200 mrad and averaging many frozen phonon configurations at 300 K. Channeling simulations were performed with the beam intensity being tracked by saving a 2D intensity map at every z slice for any given incident probe position.

Fixing known beam parameters ($E_0 = 300$ keV, $\alpha_{obj} = 24.5$ mrad, with measured spherical aberration parameters $C_{3,0} = +2\,\mu$m and $C_{5,0} = -2$ mm), probe defocus and source size were tuned to match the experimental HAADF line scans. For the example specimen data, best agreement was obtained using defocus $\Delta f = +30$ Å (positive defocus corresponds to probe focusing after the specimen surface), resulting in optical probe sizes of $d_p = 0.45$ Å, combined with a Gaussian source size function with full-width-at-half-maximum (FWHM) of 0.9 Å (Appendix A). Carefully modeled probes were used to simulate HAADF images and EDX maps, as well as for deconvolution of probe effects from the experimental data.

B. Orbital calculations

The EDX map formation was simulated by calculating the depth-integrated overlap of the probe intensity with the core orbital corresponding to a given characteristic x-ray peak [32]. All maps were simulated using a 32×32 sampling of probe positions across the cubic unit cell, with probe intensities being interpolated up to 256×256 pixel^2 per unit cell using a cubic spline routine for all data processing and analysis. More discussion on sampling can be found in Ref. [33].

Each orbital was approximated as the projected charge density of the core orbital displaced by the thermal vibration of that atom (e.g., the Ti projected $1s$ orbital smeared by a Gaussian function with isotropic standard deviation 0.035 Å for the Ti K edge and the Sr projected $2p$ orbital smeared by a Gaussian function with isotropic standard deviation 0.045 Å for the Sr L edge). The three-dimensional orbitals of atoms were calculated using the *atomic* module of the Quantum Espresso code [34] as an independent-atom relativistic density functional theory (DFT) calculation employing Perdew-Burke-Ernzerhof generalized gradient approximation (PBE-GGA) functionals [35], then converted to 2D projected orbitals by integrating them over the slice thickness.

For comparison, the first-principles excitation potential (for excitation from a core state to any allowed final state, also called the effective transition potential or optical potential) in the local approximation [36] was calculated for 300 keV electrons using the μSTEM code [37], employing the same thermal vibration amplitudes as above. This method takes into account the quantum-mechanical interactions of the incident STEM probe with atomic core-level orbitals. Depending on the core-level orbital and its binding energy (16.1 keV for Sr $1s$, 4.97 keV for Ti $1s$, 1.94–2.01 keV for Sr $2p$, and 0.454–0.460 keV for Ti $2p$) [38], there are varying degrees of broadening evident in the first-principles effective local potential, which is due to long-range Coulombic interaction between the core electrons and incident electron.

IV. RESULTS AND DISCUSSION

The x-ray maps were collected simultaneously along with HAADF images using an aberration-corrected STEM. An example of one such data set is shown in Fig. 1. Similar EDX maps of STO have been reported previously and can be routinely obtained using aberration-corrected STEMs [14,17,39].

Reliable probing of core-level electron orbitals in real-space using STEM-EDX maps hinges on two basic concepts. First, because these x rays are produced solely by filling empty states in core-level orbitals ($1s$ and $2p$ orbitals for K and L x rays, respectively), each x-ray map is really a spatially resolved measurement of core-electron excitation probability for a specific orbital, also known as the effective transition potential

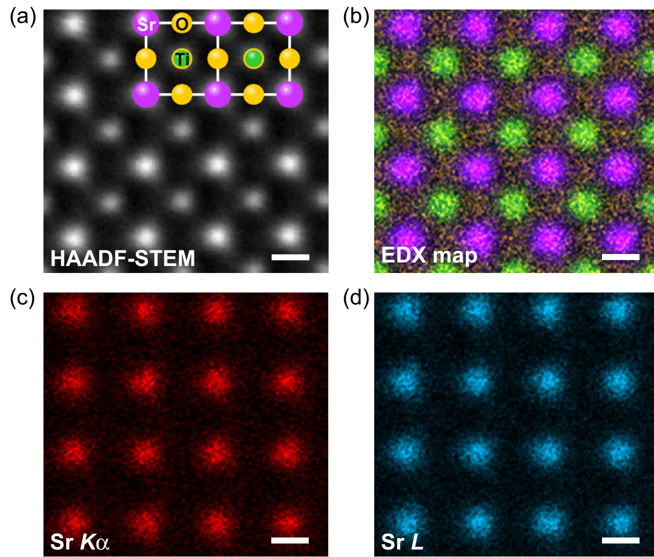

FIG. 1. (a) The HAADF-STEM image of STO viewed along the [001] crystallographic direction. A model of the atomic positions is overlaid on the image to clarify identification of atomic columns. (b) Composite STEM-EDX map of STO, superposing combined Sr $K\alpha$ and L (purple), Ti $K\alpha$ (green), and O K (yellow) maps. (c)–(d) Individual Sr $K\alpha$ (c) and Sr L (d) EDX maps. The scale bar is 2 Å. The EDX map was acquired from a single EDX mapping (with size of 32×32 Å^2), cut 2×2 into four individual 16×16 Å^2 images, and averaged using standard cross-correlation algorithm.

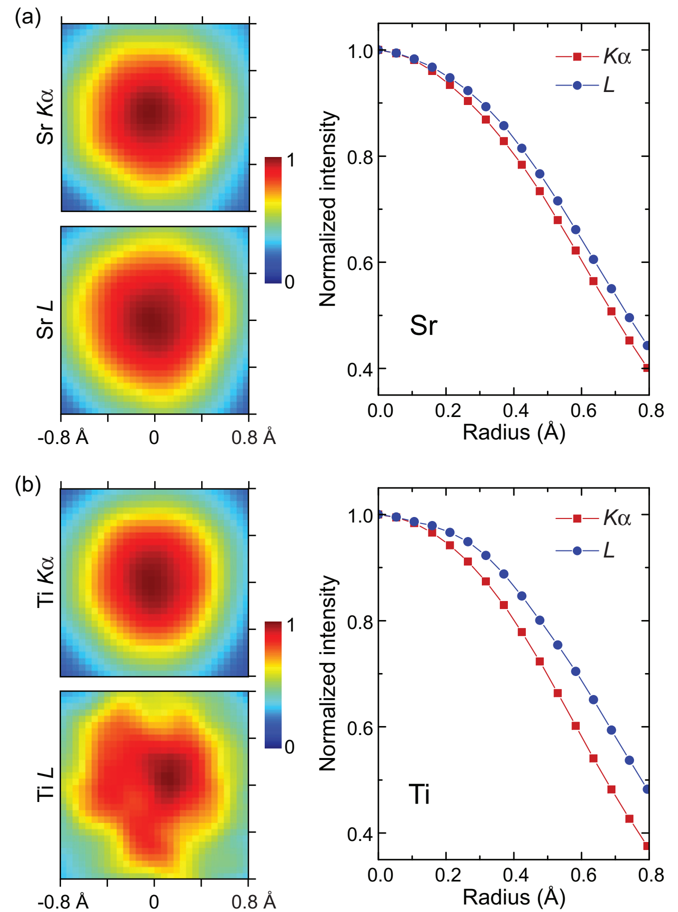

FIG. 2. (a) Individual Sr $K\alpha$ and L EDX maps from the Sr column of STO viewed along the [001] crystallographic direction. (b) Individual Ti $K\alpha$ and L EDX maps from the Ti/O column of STO viewed along the same direction. The less circular shape of the Ti L map is due to a much lower signal-to-noise ratio in the data, showing that the Ti L signal still needs to be improved. For direct comparison, maps are background subtracted and normalized to their central intensity. Azimuthally averaged radial profiles are presented at right for better comparison. These maps constitute the cross-correlated average of data from approximately 450 identical atomic columns and all obtained simultaneously in a single experiment. Note that the size difference even in the maps is visible.

or optical potential. Second, when two different x-ray maps are collected simultaneously for the same element—such as both $K\alpha$ and L from Sr atoms in Figs. 1(c) and 1(d)—it is possible to directly compare the two orbitals, as they are measured in exactly equivalent conditions: an identical incident beam (which is atomic column independent) undergoing identical propagation through the sample (which is atomic column specific). The ability to probe and record two different pairs of EDX maps from two different atoms, all under the same STEM operational conditions, makes this particularly robust and minimally sensitive to instrument variability. Using extensive low-noise data sets, it also allows confident identification of excitation delocalization effects in the EDX maps.

To increase the signal-to-noise ratio of STEM-EDX maps, many x-ray maps from identical atomic columns, all recorded in the same experiment, are cross correlated by rigid registration and averaged together [40]. The method is based on standard cross correlation aided by averaging of single column EDX maps with modifications in the reference image. It produces EDX maps with minimal specimen drift, beam drift, and scan distortions. Details of the procedure are described in Ref. [40]. An example of the resulting set of four maps—two for Sr and two for Ti—from one experiment is presented in Fig. 2. Note that the Ti L signal is sixfold weaker than Ti $K\alpha$ when x-ray counts from each elemental peak are compared: Sr $K\alpha$ (0.49×10^6), Sr L (1.08×10^6), Ti $K\alpha$ (1.09×10^6), and Ti L (0.16×10^6) in pulses from a single EDX mapping experiment, resulting in somewhat noisier and asymmetric images. Improvement of Ti L map fidelity requires either greater dose per raw map, which was rendered impractical by sample damage rate constraints, or many experiments at low dose on parts of sample, which was rendered by microscope stability. The question of uncertainties in the excitation potential measurements derived from all four EDX signals will be discussed later.

Even at the stage of cross-correlated maps, where the effects of finite source size and beam channeling are dominant, differences between $K\alpha$ and L maps are visible, as for each element the L map is systematically wider than the $K\alpha$ map. We observe such differences between $K\alpha$ and L maps in many experiments, performed on different days for different STO samples in varying operational conditions (representative results are shown in this paper, and the rest of the results can be found in the Supplemental Material [20]). Observations of the Ti L map exhibiting wider peaks than the Ti $K\alpha$ in [001]-oriented STO have independently been

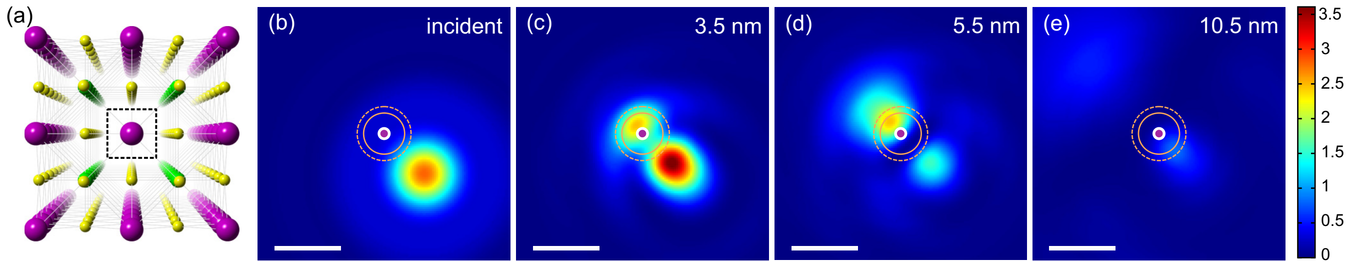

FIG. 3. (a) Perspective rendering of an atomic model of the STO crystal viewed along the [001] direction: Sr (purple), Ti (green), and O (yellow). The dashed square box indicates the area considered in channeling simulations. (b)–(e) Simulated intensities of a STEM beam located 0.4 Å away from the Sr atomic column at depths of 0.0, 3.5, 5.5, and 10.5 nm in the crystal. The position of the Sr column is indicated by the purple dot and the extents of both $1s$ and $2p$ orbitals are highlighted by the solid and dashed orange circles, respectively. The scale bar is 0.5 Å.

reported by others [39], indicating that our observations are indeed reproducible.

The $K\alpha$ and L EDX maps from the same atom (whether Sr or Ti) differ because $K\alpha$ emission results from excitations of $1s$ core-level electrons by the incident STEM probe to available states above the Fermi energy, whereas L emission results from excitations of $2p$ core-level electrons. These excitations are followed by x-ray-emitting electron relaxations to fill the newly available core-level states ($2p$ to $1s$ and $3s/3d$ to $2p$ for $K\alpha$ and L x rays, respectively), with emission being isotropic. The localization of these orbital-characteristic x rays is, therefore, constrained by the spatial extent of the core-level electron orbitals, with additional broadening due to the physics of Coulombic beam-orbital interaction that is often termed as the "impact parameter" effect [41]. The complex nature of the beam-orbital interaction producing electronic excitations from core levels has been discussed in the literature [32,36,42] and is modeled in STEM-EDX simulation software [37]. Since this quantum mechanical beam-orbital interaction is the actual experimental measurement, our imaged orbitals will include broadening due to the Coulombic nature of this interaction.

Two factors should be taken into account to understand why distinction between $1s$ and $2p$ orbitals is possible in STEM-EDX experiments with a scanning probe ∼1 Å wide, when even with the thermal vibrations of atoms by phonon modes of the crystal (the room temperature RMS atomic displacements are 0.08 and 0.06 Å for Sr and Ti atoms, respectively [31]), the effective extent of the orbitals is only 0.2–0.5 Å, calculated using the Quantum Espresso code [34]. The first factor is the interaction of the STEM beam with the orbitals. As an electron beam propagates through a crystal, it channels along atomic columns [43,44]. In addition to this well-known on-column channeling, when a focused STEM beam is placed slightly off of an atomic column, it propagates by first shifting into the atomic column and then channeling along the column [45,46]. However, a closer look at the propagation of beams located just off of an atomic column shows that while they propagate along the atomic column, they oscillate back and forth within the dimension of the atom along the column. This strong localization of off-column beams prior to dechanneling is the main reason why electron beams initially positioned outside of the core-level orbital coverage area can still produce strong characteristic K and L x-ray signals. This beam behavior is illustrated for a Sr column in STO (Fig. 3), depicting the simulated depth-varying intensity of an aberration-corrected STEM probe placed 0.4 Å away from the column using a well-established multislice code [29]. All simulation parameters necessary to describe the STEM beam and STO crystal were derived from experimental data (see Supplemental Material [20]).

Since we observe this effect for both Sr and Ti/O columns in STO and for several beam sizes (see Supplemental Material [20]), it might be a more general phenomenon. The intensity and frequency of oscillations depends on crystal structure, atomic column composition, and STEM beam parameters. When the same beam discussed in Fig. 3 is centered 0.4 Å away from the Ti/O column, it is drawn onto the column more gradually and oscillates with lower frequency than for the Sr column. Examples of this occurring in STO with various beam sizes are also obtained (see Supplemental Material [20] for videos).

The second factor that affects the visibility of the different orbitals is the aforementioned orbital excitation broadening due to Coulombic beam-orbital interaction. Because the binding energies of the core-level orbitals examined in this paper vary by more than an order of magnitude (from less than 0.5 keV for Ti $2p$ electrons to 16 keV for Sr $1s$ electrons), there is an additional broadening of orbitals in EDX mapping that is inversely proportional to the electron binding energy of that orbital. This effect can be theoretically predicted from first-principles excitation calculations [36,41].

In aberration-corrected STEM, the incident electron beam is determined by the combined effects of diffraction, the geometrical and chromatic aberrations of the lenses, and the finite demagnified source size. Detailed analysis, based on measured values of aberration coefficients, indicates that in our experiment, the probe size was approximately $d_{\mathrm{p}} = 0.45$–0.5 Å; the effective source size in the specimen plane, inferred from comparing HAADF-STEM experimental images to multislice simulations, was approximately $d_{\mathrm{ss}} = 0.9$ Å (see Appendix A). The finite size of the STEM electron source (combined with any stage and sample vibration) produces an incoherent spreading of the optical probe d_{p} by the amount d_{ss}, smearing a narrow probe over a wider area. The effects of source size on STEM-EDX maps and HAADF-STEM images can be taken into account as a simple convolution of the source distribution with the optical probe image [47]. In the experiment discussed above, the effective STEM probe size, due to the convolution of these two contributions, is approximately $d_{\mathrm{eff}} = (d_{\mathrm{p}}^2 + d_{\mathrm{ss}}^2)^{1/2} \cong 1.0$ Å.

Now, if we remove the effects of source size smearing and beam channeling from the measured EDX maps, the resulting objects are the probed core-level electron orbitals smeared due to thermal vibrations of the atoms and excitation broadening. The removal of the finite source distribution proceeds as a simple deconvolution of the estimated Gaussian source function using damped accelerated Richardson-Lucy deconvolution [48]. The removal of channeling effects (discussed in greater detail in Appendix B) was performed as follows. First, the 2D intensity distribution of STEM beams propagating through [001]-oriented STO was simulated, placing the incident beams in a square grid, spanning the unit cell just as in STEM-EDX experiments. The resulting five-dimensional (5D) data array contains 2D beam intensities at each depth in the crystal (the frames in Fig. 3 are examples for one beam position at different depths), generated for every beam position in the 2D map. By averaging 2D beam intensities over the experimentally determined sample thickness, the 5D data array is condensed into a four-dimensional (4D) array. Finally, by mathematically solving this complex linear system—the simulated 4D array operating on an unknown 2D orbital object to form the experimentally measured 2D x-ray map—the effects of beam channeling can be removed, yielding a measurement of the probed core-level orbital excitation potential associated with that x-ray peak. Owing to the ill-posed problem of inverting the system of equations to remove the effects of the channeled probe, the system was nonuniquely solved by comparing spectrum images simulated using physically sound trial solutions against the experimental spectrum images. Best-fitting trial solutions were selected based on least-squared error analysis (Appendix C).

The final results of removing combined source size and beam channeling effects, performed on the EDX maps, shown in Fig. 2 (see Appendices B and C for details), are presented in Fig. 4. The measured core-level electron orbital excitation potentials are comparable to the theoretical predictions. The first-principles calculations of projected orbital radial profiles, both with (excitation potential in the local approximation) and without (projected charge density) excitation broadening [36,37], are presented in Fig. 5 alongside the experimentally determined excitation potentials. Not only are the overall sizes of the experimentally measured excitation potentials for each orbital in agreement with predictions, but also those for $1s$ orbitals are systematically smaller in size than for $2p$ orbitals for both Sr and Ti atoms. Similar results were observed in the analysis of other independent data sets (see Supplemental Material [20]). Discrepancy, especially in the tails of the excitation potentials, might originate from complex subtleties of the experimental source distribution, which are not reflected in the Gaussian source distribution used for probe deconvolution calculations. It is also unknown whether the limited signal-to-noise and sampling resolution of the raw experimental maps caused any subtle distortions of the high-quality cross-correlated maps, an effect which could propagate to the experimentally derived excitation potentials.

Taking the analysis one step further, these experimental results are used to measure impact parameters of the core-level electronic excitations responsible for x-ray generation. The impact parameter, or delocalization of the excitations beyond the extent of the initial state, is determined by the range of

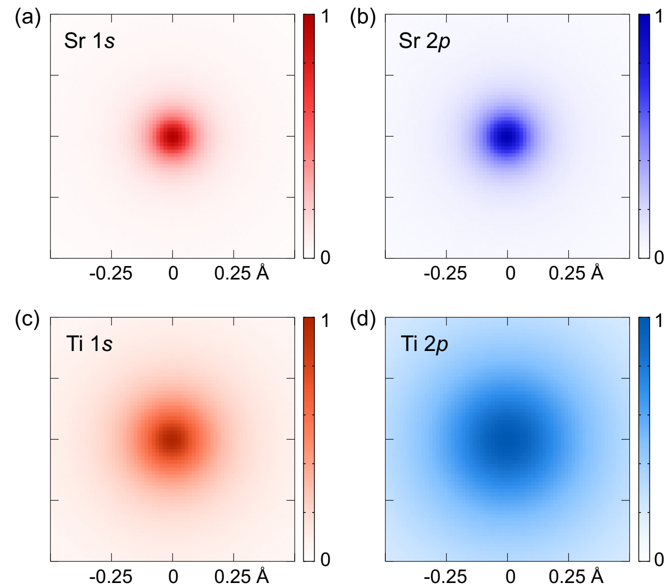

FIG. 4. (a)–(d) Experimentally observed projected excitation potentials for $1s$ and $2p$ orbitals of Sr and Ti, including the effects of atomic thermal vibrations and excitation broadening, retrieved from the EDX maps in Fig. 2.

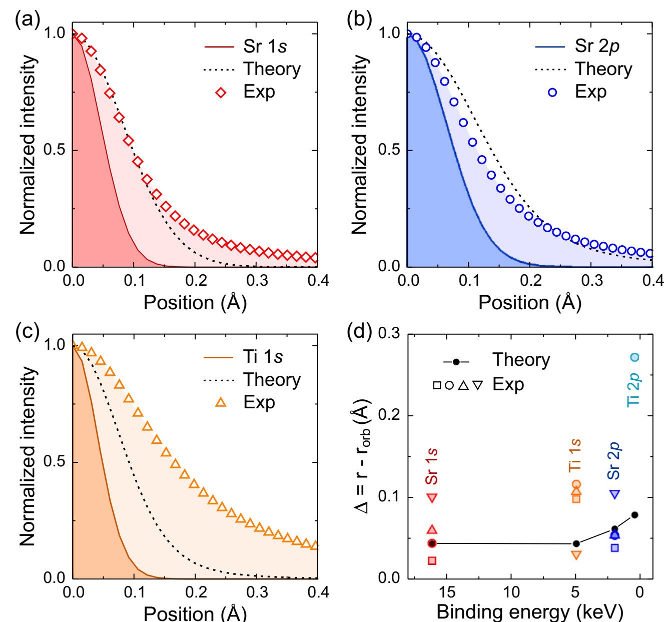

FIG. 5. (a)–(c) Comparison of the radial distribution of experimentally observed and calculated excitation potentials, alongside calculated projected charge densities for $1s$ and $2p$ orbitals of Sr and Ti. Theoretical calculations include the effects of atomic thermal vibrations. Calculations with excitation broadening are indicated by dashed black lines and those without excitation broadening by solid colored lines. (d) Measured impact parameters of the electronic excitations for all four orbitals. The theoretical predictions are also shown for comparison. Experimental data are from four individual experiments using three different STO samples, except Ti $2p$, which is from one set of experiment as other sets produced insufficient signal-to-noise ratio data (each symbol represents a different experiment).

nonvanishing values of the square of the electronic transition matrix element due to the Coulombic beam-orbital interaction, V:

$$M^2 = |\langle \Psi_f|\hat{V}|\Psi_i\rangle|^2.$$

It can be estimated by evaluating differences between the radii of measured projected excitation potentials r and those of the exact projected charge densities of core orbitals r_{orb}: $\Delta = r - r_{\mathrm{orb}}$. The analysis based on results from this and additional three individual measurements are presented in Fig. 5(d), and the results are compared to theoretical predictions. The data indicate that for core orbitals with a rather wide range of binding energies (2 to 16 keV), the electronic excitation impact parameter is $\leqslant 0.1$ Å. For orbitals with binding energies smaller than 2 keV, impact parameters increase but are still smaller than approximately 0.3 Å (for the Ti $2p$ orbital at 0.4 keV). As was discussed earlier, the Ti L EDX map has a lower signal-to-noise ratio resulting in a less accurately determined impact parameter of 0.3 Å, which is significantly off from the theoretical prediction.

The uncertainties in the estimation of the STEM beam parameter, sample thickness, source size, and shape, as well as the neglect of unavoidable minor electron beam damage of specimen and approximation-induced error in beam channeling simulations and theoretical calculations of excitation broadening, will produce small errors and, in turn, limit the accuracy of core-level orbital measurements. Note that having a high signal-to-noise ratio in the original EDX maps is the essential factor allowing for distinction of small size differences between $1s$ and $2p$ orbitals (0.1 and 0.4 Å for Sr and Ti, respectively), going beyond the conventionally defined resolution of the STEM. However, note that analogous statistically driven enhancement of measurement precision is often practiced and has been demonstrated for ADF-STEM imaging [49].

V. CONCLUSIONS

We have shown that by recording EDX maps from crystalline specimens using an aberration-corrected STEM equipped with a high-efficiency x-ray detection system, it is ultimately possible to probe core-level electron orbitals in real space. In the case of STO, both the $1s$ and $2p$ orbitals of Sr and Ti atoms are probed; as expected, $1s$ orbitals are always smaller than $2p$ orbitals, and all orbitals are localized on their respective atomic columns. This method should be applicable to any atomic columns in any crystal, and it is limited only by uncertainties in experimental parameters, as well as by the rate of x-ray collection relative to electron beam damage of the specimen. We also have shown that these experiments allow accurate measurements of the electronic excitation impact parameters due to Coulombic beam-orbital interaction, at 300 keV ranging from around 0.1 Å for deeply bound Sr $1s$, Ti $1s$, and Sr $2p$ orbitals, to about 0.3 Å for more weakly bound Ti $2p$ core orbitals. Similarly, it will be possible to probe core-level electron orbitals and measure impact parameters using core-loss EELS mapping in an aberration-corrected STEM, provided that a large collection aperture is used (to ensure a well-localized excitation potential) [42]. The results and approach presented demonstrate a precision of electron beam-based spectroscopy that is limited only by the impact parameter of excitation. They may also be extended to improve the spatial localization of STEM-EDX elemental composition measurements by deconvolving probe channeling, which should also be applicable for the analysis of any well-localized spectroscopy.

ACKNOWLEDGMENTS

This paper was supported, in part, by the National Science Foundation (NSF) under Award No. DMR-1006706 and NSF Materials Research Science Engineering Center (MRSEC) under Awards No. DMR-0819885 and No. DMR-1420013. The STEM analysis was carried out in the Characterization Facility of the University of Minnesota, which receives partial support from the NSF through the MRSEC program. Multi-slice computer simulations were performed using resources provided by the Minnesota Supercomputing Institute. The authors thank Dr. E. Ebbini for many critical discussions and guidance with multidimensional deconvolution algorithms, Dr. P. Batson and P. Kumar for helpful discussions, and Dr. M. Topsakal and Dr. R. Wentzcovitch for providing density functional theory calculations that have influenced the course of the analysis. We also thank Dr. F. Bates, Dr. C. Leighton, Dr. D. Hickey, and Dr. D. Flannigan for critically reading the manuscript.

J.S.J. and M.L.O. contributed equally to this work.

APPENDIX A: EFFECTIVE SOURCE SIZE

The effective probe size, d_{eff}, (the size of the "finite source" probe) determining HAADF-STEM images includes source size broadening, d_{ss}. To ensure accurate processing of EDX maps, both the optical probe size, d_{p}, (the size of the "point source" probe) and the source size broadening (also referred to as "finite source broadening") must be determined. The optical probe size for each experiment is determined by measuring experimental parameters of the microscope. The source size is estimated by comparing simulated and experimental HAADF-STEM images.

To elucidate the effect of source size broadening, probes with different optical probe sizes were generated and used in multislice code to simulate HAADF-STEM images at specimen thicknesses corresponding to each experiment. Different widths of Gaussian finite source broadening were applied to simulate HAADF-STEM images with varying source size at each thickness; the FWHMs of Sr columns in simulated HAADF-STEM images are presented as contour maps, depending on both the optical probe size and source size in Fig. 6(a). The experimental optical probe sizes were estimated using the CEOS DCOR probe corrector software (see Supplemental Material [20]), and they are conservatively in the range of $d_{\mathrm{p}} = 0.45$–0.55 Å. As can be seen from Fig. 6(a), the measured Sr column sizes are mostly governed by the source size broadening, being weakly sensitive to the optical probe size for the $\sim$1 Å effective source sizes observed in these experiments.

HAADF-STEM image simulations applying the inferred source size broadening to the point source image are in excellent agreement with experimental HAADF-STEM images,

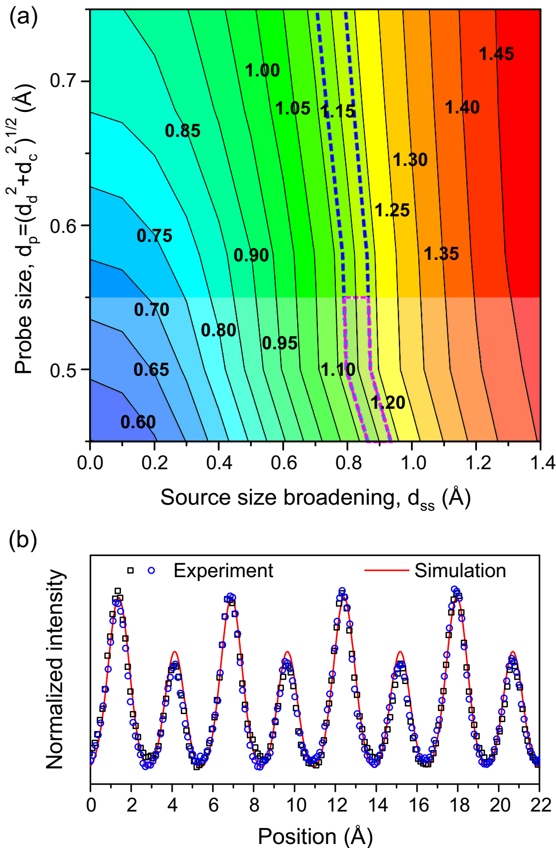

FIG. 6. (a) Estimated Sr column size vs optical probe size vs source size broadening from the example specimen data. Optical probe size ranges were based on measurements made by the probe corrector software and are indicated by the transparent box. Measured Sr column size ranges in HAADF-STEM images are indicated by the windows marked by the blue dotted lines: 1.12–1.18 Å. The range of possible parameters is indicated by the pink dotted lines. (b) Line profile comparison between the experiment and simulation. The line profile was taken along the ⟨110⟩ direction in the HAADF images. Simulation was conducted using the optical probe size and source size broadening inferred from (a). Both experimental and simulated line profiles were background subtracted before normalizing to their respective maxima.

as illustrated by line profile comparisons in Fig. 6(b). The best-fitting values for optical probe size and source size are $d_p = 0.45$ Å and $d_{ss} = 0.9$ Å. In other experiments performed on different samples on different days, the values were ($d_p = 0.45$ Å and $d_{ss} = 1.1$ Å) and ($d_p = 0.45$ Å and $d_{ss} = 1.2$ Å); see Supplemental Material [20].

APPENDIX B: DECONVOLVING CHANNELING ELECTRON BEAM

Core-level orbitals can be determined by deconvolving channeled STEM probes from source-removed EDX maps, a notion that has also been discussed by others [16,18]. The EDX intensity for a given probe position can be evaluated as the convolution of depth-integrated channeling intensity for that probe position with the orbital excitation potential. We evaluated 32 × 32 probe positions across the unit cell, sampling both the object and depth-integrated probe intensity using 256 × 256 pixel^2 per unit cell grid using multislice code. Deducing the atomic orbitals producing EDX maps then requires solving the following system of equations:

$$O(i,j) \otimes P(i,k,j,l) = \mathrm{EDX}(k,l), \quad \text{(B1)}$$

where $O(i,j)$ is the 2D orbital projection on the discrete unit cell grid (i,j), $P(i,k,j,l)$ is the 4D channeled probe array for a given thickness, and $\mathrm{EDX}(k,l)$ is the experimentally measured 2D EDX map (source size removed) at a probe position (k,l). Here, $\otimes$ denotes a 2D convolution operation over (i,j).

In this paper, this amounts to solving an underconstrained linear system: using simulated probe data $P(i,k,j,l)$ (known intensities depth integrated at each of the 65 536 sample points, for each of the 1024 probe positions) and known source-removed experimental spectrum image data (known intensities for each of the 1024 probe positions), we determine the unknown orbitals (unknown value for all of the 65 536 sample points).

This problem can be "unbiasedly" solved by inverting the system to solve for the potential. One classic method for minimum-norm, least-squares solution of this system is the Moore-Penrose pseudoinverse [50], which can be tuned by limiting the spread of a matrix's singular values [51] that are allowed to contribute to the solution. Iterative least-squares methods for inverting nonsquare matrices also exist, such as the conjugate-gradient-type sparse linear equation and least squares (LSQR) algorithm [52]. Both the Moore-Penrose and LSQR methods were employed, as implemented in MATLAB, to calculate orbital excitation potentials for each of the data sets; however, when noise is amplified in the solution (by increasing the number of singular values allowed in Moore-Penrose or by increasing the number of iterations of LSQR), the squared-error of the solution decreases even as physically absurd features emerge in the solution (see Supplemental Material [20]).

Robustly converging iterative approaches, based on "projection onto convex sets" [53], were also considered. However, they were abandoned in favor of a simpler, if more overtly biased, approach: using trial solutions with a physically sensible form. Both Moore-Penrose and LSQR methods yield Lorentzian-like solutions at intermediate tolerance levels, and Lorentzian parameterization is standard for deeply bound orbital excitation potentials [54], motivating the examination of Lorentzian trial solutions. Because thermal vibrations in the solid have approximately Gaussian distribution, all Lorentzians were first convolved with Gaussians corresponding to their RMS thermal vibrations to generate Lorentzian-form trial solutions (e.g., a 0.10 Å Lorentzian trial solution for the Sr column is a Lorentzian with FWHM 0.10 Å convolved with a Gaussian of standard deviation 0.045 Å).

APPENDIX C: SELECTING BEST-FITTING SOLUTIONS FOR CORE-LEVEL ORBITALS

The fitness of a solution is conventionally determined by the average square error, often represented as the RMS error (RMSE). For any image $I(i,j)$ fitted by a function $F(i,j)$,

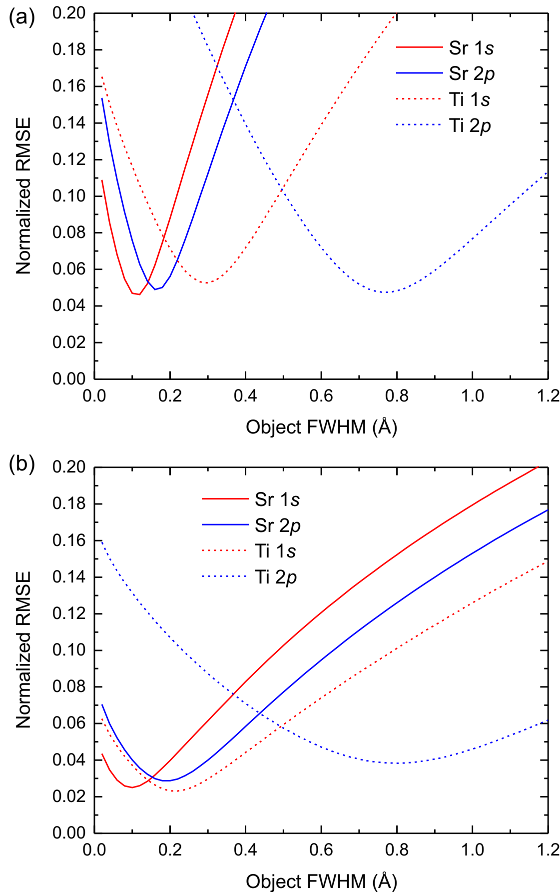

FIG. 7. Reconstructed image RMSE as a function of Lorentzian trial object size: (a) point source conditions and (b) finite source conditions. Both measures give similar sizes of the best-fitting object, although the RMSE varies more strongly as a function of object size in point source conditions.

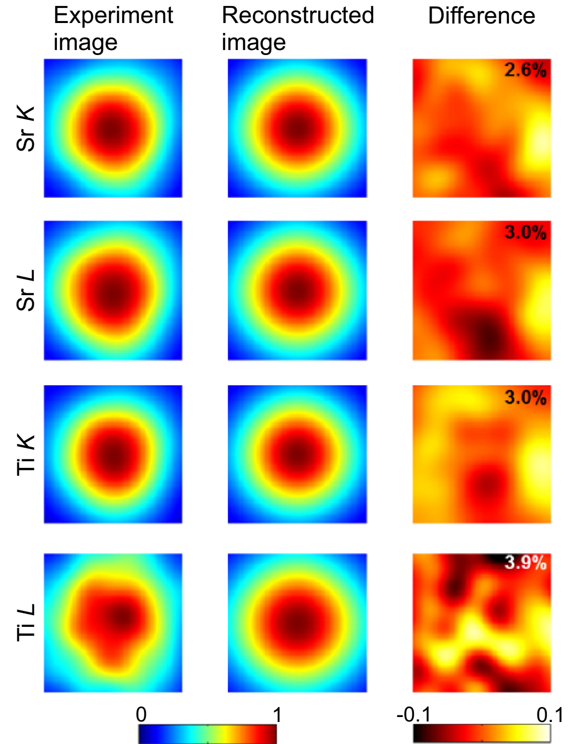

FIG. 8. Lorentzian best-fit solutions based on point source conditions, compared in finite source conditions. Normalized RMSE of best-fitting solution given in top right corner of each difference image. All plots span $^1/_2 \times {}^1/_2$ unit cell in area, centered on the column.

both discretely sampled over a number of positions $n \times m$, the RMSE is defined as follows:

$$\mathrm{RMSE} = \sqrt{\frac{\sum_{i=1}^{n} \sum_{j=1}^{m} [F(i,j) - I(i,j)]^2}{n \times m}}. \quad \text{(C1)}$$

Minimizing RMSE, either in (a) comparing point source reconstructed images to experimental source-removed images or (b) comparing finite source reconstructed images to source-inclusive experimental images, is the most straightforward objective measure for a best-fit solution. Because any constant offset in experimental data vis-a-vis reconstructed image data can corrupt the RMSE minimum (i.e., due to instrumental background in the data), all images are background-subtracted before comparisons are made. The centering of both experimental and reconstructed images was also verified to ensure accurate RMSE calculation.

Because RMSE between experimental and reconstructed images is more sensitive to object size for point source than finite source comparisons (Fig. 7), we made best-fit determinations by comparing point source reconstructed images to their source-removed experimental counterparts, evaluating RMSE over a quarter of the unit cell ($^1/_2 \times {}^1/_2$ unit cell region centered on a given column). Error analysis (plots of RMSE vs Lorentzian FWHM and summaries of best-fit solution images compared to experimental images in finite source conditions) is presented in Figs. 7 and 8, respectively (see Supplemental Material [20]). Thus, these are the solutions presented in Fig. 4. Note that because such ill-posed problem was addressed by assuming physically sensible forms for both the source size (Gaussian) and excitation potentials (Lorentzian blurred by thermal vibration Gaussian), the solutions are smooth, as shown in Fig. 4.

[1] P. Coppens, *X-Ray Charge Densities and Chemical Bonding* (Oxford University Press, New York, 1997).
[2] J. M. Zuo, M. Kim, M. O'Keeffe, and J. C. H. Spence, Nature (London) **401**, 49 (1999).
[3] J. M. Zuo, Rep. Prog. Phys. **67**, 2053 (2004).
[4] P. N. H. Nakashima, A. E. Smith, J. Etheridge, and B. C. Muddle, Science **331**, 1583 (2011).
[5] T. Eguchi, Y. Fujikawa, K. Akiyama, T. An, M. Ono, T. Hashimoto, Y. Morikawa, K. Terakura, T. Sakurai, M. G. Lagally, and Y. Hasegawa, Phys. Rev. Lett. **93**, 266102 (2004).
[6] L. Gross, F. Mohn, N. Moll, P. Liljeroth, and G. Meyer, Science **325**, 1110 (2009).
[7] H. J. Lee and W. Ho, Science **286**, 1719 (1999).

[8] C. Weiss, C. Wagner, R. Temirov, and F. S. Tautz, J. Am. Chem. Soc. **132**, 11864 (2010).
[9] M. Haider, S. Uhlemann, E. Schwan, H. Rose, B. Kabius, and K. Urban, Nature (London) **392**, 768 (1998).
[10] P. E. Batson, N. Dellby, and O. L. Krivanek, Nature (London) **418**, 617 (2002).
[11] K. Kimoto, T. Asaka, T. Nagai, M. Saito, Y. Matsui, and K. Ishizuka, Nature (London) **450**, 702 (2007).
[12] D. A. Muller, L. F. Kourkoutis, M. Murfitt, J. H. Song, H. Y. Hwang, J. Silcox, N. Dellby, and O. L. Krivanek, Science **319**, 1073 (2008).
[13] M. W. Chu, S. C. Liou, C. P. Chang, F. S. Choa, and C. H. Chen, Phys. Rev. Lett. **104**, 196101 (2010).
[14] A. J. D'Alfonso, B. Freitag, D. Klenov, and L. J. Allen, Phys. Rev. B **81**, 100101 (2010).
[15] N. R. Lugg, M. Haruta, M. J. Neish, S. D. Findlay, T. Mizoguchi, K. Kimoto, and L. J. Allen, Appl. Phys. Lett. **101**, 183112 (2012).
[16] M. J. Neish, N. R. Lugg, S. D. Findlay, M. Haruta, K. Kimoto, and L. J. Allen, Phys. Rev. B **88**, 115120 (2013).
[17] G. Kothleitner, M. J. Neish, N. R. Lugg, S. D. Findlay, W. Grogger, F. Hofer, and L. J. Allen, Phys. Rev. Lett. **112**, 085501 (2014).
[18] N. R. Lugg, M. J. Neish, S. D. Findlay, and L. J. Allen, Microsc. Microanal. **20**, 1078 (2014).
[19] L. J. Allen, A. J. D'Alfonso, B. Freitag, and D. O. Klenov, Mater. Res. Bull. **37**, 47 (2012).
[20] See Supplemental Material at http://link.aps.org/supplemental/10.1103/PhysRevB.93.165140 for the details of the materials, methods, electron beam channeling movies, and more results.
[21] P. M. Voyles, J. L. Grazul, and D. A. Muller, Ultramicroscopy **96**, 251 (2003).
[22] R. F. Egerton, *Electron Energy-Loss Spectroscopy in the Electron Microscope* (Springer, New York, 2011).
[23] K. A. Mkhoyan, T. Babinec, S. E. Maccagnano, E. J. Kirkland, and J. Silcox, Ultramicroscopy **107**, 345 (2007).
[24] J. M. LeBeau, S. D. Findlay, L. J. Allen, and S. Stemmer, Phys. Rev. Lett. **100**, 206101 (2008).
[25] H. S. v. Harrach, P. Dona, B. Freitag, H. Soltau, A. Niculae, and M. Rohde, J. Phys.: Conf. Ser. **241**, 012015 (2010).
[26] W. H. Press, S. A. Teukolsky, W. T. Vetterling, and B. P. Flannery, *Numerical Recipes: The Art of Scientific Computing* (Cambridge University Press, New York, 2007).
[27] M. A. O'Keefe, P. R. Buseck, and S. Iijima, Nature (London) **274**, 322 (1978).
[28] E. J. Kirkland, R. F. Loane, and J. Silcox, Ultramicroscopy **23**, 77 (1987).
[29] E. J. Kirkland, *Advanced Computing in Electron Microscopy* (Springer, New York, 2010).
[30] R. F. Loane, P. Xu, and J. Silcox, Acta Crystallogr. Sec. A **47**, 267 (1991).
[31] B. C. Chakoumakos, Physica B **241-243**, 361 (1997).
[32] L. J. Allen and T. W. Josefsson, Phys. Rev. B **52**, 3184 (1995).
[33] C. Dwyer, Ultramicroscopy **110**, 195 (2010).
[34] P. Giannozzi, S. Baroni, N. Bonini, M. Calandra, R. Car, C. Cavazzoni, D. Ceresoli, G. L. Chiarotti, M. Cococcioni, I. Dabo, A. D. Corso, S. de Gironcoli, S. Fabris, G. Fratesi, R. Gebauer, U. Gerstmann, C. Gougoussis, A. Kokalj, M. Lazzeri, L. Martin-Samos *et al.*, J. Phys.: Condens. Matter **21**, 395502 (2009).
[35] J. P. Perdew, K. Burke, and M. Ernzerhof, Phys. Rev. Lett. **77**, 3865 (1996).
[36] M. P. Oxley and L. J. Allen, Phys. Rev. B **57**, 3273 (1998).
[37] L. J. Allen, A. J. D'Alfonso, and S. D. Findlay, Ultramicroscopy **151**, 11 (2015).
[38] A. Thompson, D. Attwood, E. Gullikson, M. Howells, J. Kortright, and A. Robinson, *X-Ray Data Booklet* (Lawrence Berkeley National Laboratory, University of California, Berkeley, CA, 2009).
[39] P. Lu, E. Romero, S. Lee, J. L. MacManus-Driscoll, and Q. Jia, Microsc. Microanal. **20**, 1782 (2014).
[40] J. S. Jeong and K. A. Mkhoyan, Microsc. Microanal. (2016), doi:10.1017/S1431927616000635
[41] M. P. Oxley and L. J. Allen, Ultramicroscopy **80**, 125 (1999).
[42] E. C. Cosgriff, M. P. Oxley, L. J. Allen, and S. J. Pennycook, Ultramicroscopy **102**, 317 (2005).
[43] J. Fertig and H. Rose, Optik **59**, 407 (1981).
[44] R. F. Loane, E. J. Kirkland, and J. Silcox, Acta Crystallogr. Sec. A **44**, 912 (1988).
[45] J. Etheridge, S. Lazar, C. Dwyer, and G. A. Botton, Phys. Rev. Lett. **106**, 160802 (2011).
[46] K. Watanabe, T. Yamazaki, Y. Kikuchi, Y. Kotaka, M. Kawasaki, I. Hashimoto, and M. Shiojiri, Phys. Rev. B **63**, 085316 (2001).
[47] J. M. Cowley, J. Electron Microsc. Tech. **3**, 25 (1986).
[48] D. S. C. Biggs and M. Andrews, Appl. Opt. **36**, 1766 (1997).
[49] A. B. Yankovich, B. Berkels, W. Dahmen, P. Binev, S. I. Sanchez, S. A. Bradley, A. Li, I. Szlufarska, and P. M. Voyles, Nat. Commun. **5**, 4155 (2014).
[50] R. Penrose, Math. Proc. Cambridge Philos. Soc. **51**, 406 (1955).
[51] G. Golub and W. Kahan, J. SIAM. Numer. Anal. Ser. B **2**, 205 (1965).
[52] C. C. Paige and M. A. Saunders, ACM Trans. Math. Softw. **8**, 43 (1982).
[53] H. Bauschke and J. Borwein, SIAM Rev. **38**, 367 (1996).
[54] M. P. Oxley and L. J. Allen, Acta Crystallogr. Sec. A **56**, 470 (2000).